GT2008-50877

TIME ACCURATE SIMULATIONS OF A COUNTER-ROTATING ASPIRATED COMPRESSOR

Robert D. Knapke[*]
Mark G. Turner, Michael G. List,
Daniel S. Galbraith
Department of Aerospace Engineering
University of Cincinnati
Cincinnati, Ohio

Tim Beach
AVETEC Inc.
Springfield, OH

Ali A. Merchant
Gas Turbine Laboratory
Department of Aeronautics and Astronautics
Massachusetts Institute of Technology
Cambridge, MA

ABSTRACT

The 3D time accurate simulation of the MIT counter-rotating aspirated compressor is presented. The unsteady solver, TURBO, has been used with a phase-lag boundary condition to solve for the two counter-rotating rotors. An inlet boundary condition has been imposed to simulate the swirl and loss of the IGV. Cases with and without aspiration have been simulated. Comparison with data of the aspirated solution is good, especially near the tip picking up detailed features of the measured profile. On a 1D basis, the experimental efficiency is 87.9%, and the aspirated simulation is 89.4%. A comparison between the aspirated and non-aspirated simulations show the aspirated simulation is 2.2% higher in efficiency than the non-aspirated case. Flow details of the time-averaged solution in the second rotor show dramatic radial migration of high entropy fluid from the tip that gets ingested into the suction slot. This and other flow details shed light on the details of the counter-rotating aspirated design.

NOMENCLATURE

A_r Radial area
A_z Axial area
C_1 Sutherlands Constant 1
C_2 Sutherlands Constant 2
$\dot{m}$ Mass flow rate
M_i Molecular weight

PR Total Pressure Ratio
R_{gas} Specific gas constant
T_{ref} Temperature
TR Total Temperature Ratio
V_r Radial velocity
V_{ref} Reference velocity
V_z Axial velocity
X_i Molar fraction
γ Ratio of specific heats
η Efficiency
ρ Density
$\hat{}$ Derived quantity

INTRODUCTION

During the comment period of a session at the 2007 IGTI meeting in Montreal, John Denton said, "After looking at unsteady solutions, I'll never believe a steady solution again." Whereas this statement might be a bit strong and diminishes some of the design gains and understanding made with steady codes, it does represent an attitude that unsteady methods are needed to understand and simulate blade row interactions that are inherently unsteady. To that end, this paper presents an unsteady simulation of the MIT counter-rotating aspirated compressor, and compares with experimental data and a steady average passage prediction. It also compares a simulation with and without aspiration. Attention to detail of the experiment has been

[*]Address all correspondence to this author. Email: knapkerd@email.uc.edu

made, and a gleaning of understanding of the flow features is presented. The purposes of this simulation have been to accurately model the compressor, and to understand some of the flow physics inherent in the design observed and discussed in the paper by Kerrebrock, et al. [1].

The counter-rotating design allows for the elimination of the stator blade row in between rotors, which lowers the weight of the engine. A preliminary design study by Merchant, et al. [2] discusses the design of a counter-rotating fan. This study used a one-dimensional model of the fan to optimize key parameters. One of these key parameters is the speed of the second rotor, which has a large impact on the fan efficiency. The study discusses the lowering of the tip speed of the second rotor because of the high incoming Mach number. Lowering the tip speed causes higher loading. Aspiration has been used to offset the negative effects of higher loading.

The effect of aspiration on the boundary layer and turbomachinery blade performance is discussed at length by Merchant [3]. By placing the aspiration slot at the location of nearly separated flow, a smaller amount of aspiration can have a large effect on the boundary layer. This larger impact on the boundary layer in turn allows for higher blade loading. This reduction of loading is utilized in the second of the two counter-rotating rotors.

The MIT Gas Turbine Laboratory conducted the experimental testing of the Counter-Rotating Aspirated Compressor (CRAC) stage as described by Parker [4]. The CRAC rig included an inlet guide vane and two counter-rotating rotors, the second of which included aspiration. The blade counts are 35, 20 and 29, respectively. The experiment was conducted in a blowdown test facility depicted in Figure 1. During the testing, the working fluid is released by the fast-acting valve in approximately 50 ms. The fluid travels through the test section and into the dump tank. The test ends after approximately 100ms. For this testing, a mixture of argon and CO_2 with γ comparable to that of air was used as the working fluid to reduce the mechanical stresses.

The MIT test rig utilized a section of instrumentation upstream and downstream of the CRAC compressor test section. The upstream instrumentation consisted of six instrument windows set up as three pairs separated by 120 degrees. One window from each of the pairs contained a total temperature, total pressure and wall static pressure probe and one window contained a pitot probe. Also, rakes of total temperature and total pressure were located upstream of the IGV. Similar instrumentation was positioned downstream of Rotor 2 again with 6 instrument windows. Two sets of total temperature and total pressure rakes were positioned in this downstream set of instrumentation. The instrumentation is discussed in more detail by Parker [4]. The upstream experimental readings were used to determine the inlet boundary conditions for the CRAC simulation and the downstream readings were used for simulation to experimental com-
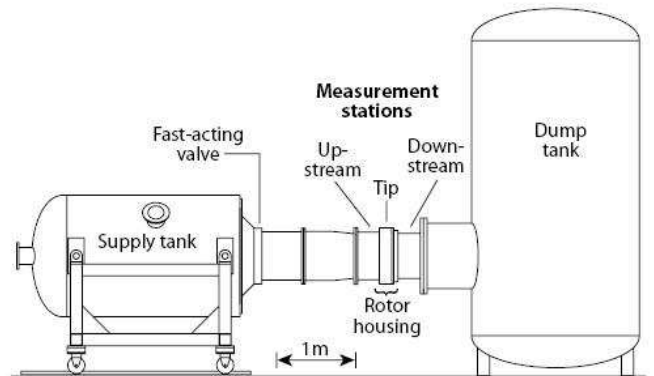
parison.

Figure 1. CRAC BLOWDOWN TEST FACILITY.

Kerrebrock, et al. [1] discuss the CRAC design. The objectives of the CRAC design were a 3:1 pressure ratio and adiabatic efficiency of 87%. The IGV introduces a counter-swirl into the high tip speed (1450 feet/sec) first rotor. The first rotor is followed by a counter rotating low speed (1150 feet/sec) second rotor. Due to the lower solidity and low tip speed of the second rotor, the loading is higher than conventionally seen for a compressor blade. This second rotor uses aspiration to remove low-momentum flow from the boundary layer to counteract the higher than conventional loading.

The wheel speeds of the two counter-rotating rotors being used for the simulation discussed in this paper were 12600 and 10020 rpm respectively. For this simulation, the molar percentage of the working fluid is 48.91% CO_2 and 51.09% argon. Although the mixture provided the same γ as air, the gas constant is not the same. The equation used to calculated the specific gas constant of the mixture is

$$R_{gas} = \sum X_i R_{gas,i} \tag{1}$$

The gas constant was found to be $198.7 \frac{J}{kgK}$ compared to air which is $287.0 \frac{J}{kgK}$. This gas constant is used for normalization and to calculate the reference velocity, which is an input into the TURBO solver:

$$V_{ref} = \sqrt{R_{gas} T_{ref}} \tag{2}$$

Another property of the gas mixture different to that of air is the variation of viscosity with temperature. TURBO uses two

Sutherlands constants as required by the following equation:

$$\mu = \frac{C_1 T^{3/2}}{T + C_2} \qquad (3)$$

Where C_1 has units of $\frac{Pa-s}{\sqrt{K}}$ and C_2 has units of K. Using known Sutherlands constants for CO_2 and data on the viscosity of Argon with varying temperature the viscosity of the mixture for several temperatures were calculated as

$$\mu_{mixture} = \frac{\sum X_i \mu_i \sqrt{M_i}}{\sum X_i \sqrt{M_i}} \qquad (4)$$

Following the computation of the viscosity of the mixture, a curve fit was placed onto the data points using Eq.(3) in order to determine the Sutherlands constants for the mixture. A plot of the viscosity for varying temperature for argon, CO_2, air and the mixture from the CRAC testing are shown in Figure 2. From this figure it can be seen that the mixture viscosity's variation with temperature is near that of air. The Sutherlands constants for the gases are shown in Table 1
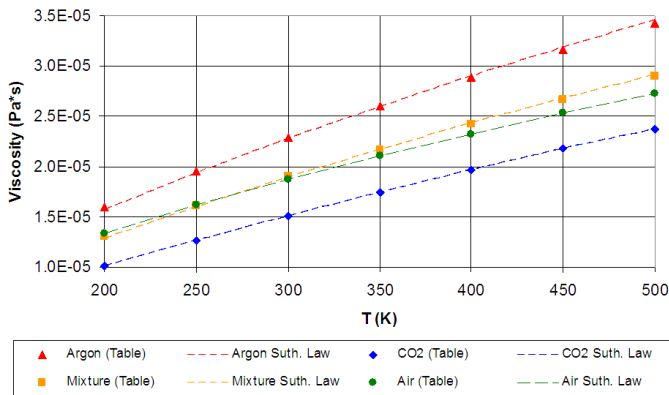
Table 1. SUTHERLANDS CONSTANTS FOR SEVERAL GASES.

	C_1 ($\frac{Pa-s}{\sqrt{K}}$)	C_2 (K)
CO_2	2.09E-6	240
Argon	1.57E-6	176
Mixture	1.83E-6	201
Air	1.51E-6	120

Figure 2. VISCOSITY OF SEVERAL GASES FOR VARYING TEMPERATURES.

NUMERICAL APPROACH

TURBO, the solver used to simulate the CRAC rig , is a 3-D, viscous, unsteady RANS solver that has been described by Chen and Whitfield [5], Chen, et al. [6–8], and Chen and Briley [9]. It employs a finite volume Roe scheme to obtain up to third order spatial accuracy and an implicit time integration to obtain up to second order temporal accuracy. The 2-equation turbulence model, the NASA/CMOTT $k - \varepsilon$ model, has been specially developed for turbomachinery calculations by Zhu, et al. [10]. TURBO integrates to the wall in the case of $y^+ < 1$ and otherwise uses wall functions. The turbulence model includes a near-wall damping term which allows the use of the $k - \varepsilon$ model at this resolution. Turbo has been shown to run on 8996 processors using MPI.

Phase-lag methodologies offer solutions restricted to the neighboring blade row's blade passing frequency and higher harmonics. Due to the blade counts of the two rotors (20 and 29), running a periodic simulation would require the modeling of the full annulus. The decision to run a single phase-lag simulation was made to reduce the computing power and computational time required. Moreover, in the interest of reducing the computation, the IGV blade row was not part of the simulation. Instead of simulating the IGV passage, a swirl profile and loss were introduced into the inlet of Rotor 1. This profile came from a solution of the IGV using TURBO.

Experience in running TURBO and comparison with rig data has been gained and presented by Gorrell et al. [11], List [12, 13] and Turner et al. [14]. This experience, along with the interpretation of results, has guided the gridding and running of the code.

Computational Grid

The computational grids used in this study were single block H-grids. The Turbomachinery Gridding System (TGS) [15] was used to create elliptically smoothed meshes for each blade passage. One H-grid block was used for each rotor passage and a third pure H-grid block was merged onto the second rotor block. This third block allowed for the capture of downstream features and it placed grid cells in the vicinity of the instrumentation rakes in the CRAC rig. The computational domain is depicted in Figure 3 with the rotors displayed in blue and the hub in red.

The number of cells in each of the two rotor passages are listed in Table 2. Both of the rotors were designed with flat trailing edges. Particular attention was paid to the spacing around the trailing edge as well as the gridlines exiting the blade passage to ensure that the cell sizes were not changing rapidly. The leading edges at midspan are shown in Figure 4 and the detail around the trailing edge (also midspan) of the grids is depicted in Figure 5. There are 8 cells in the tip gap for both Rotor 1 and
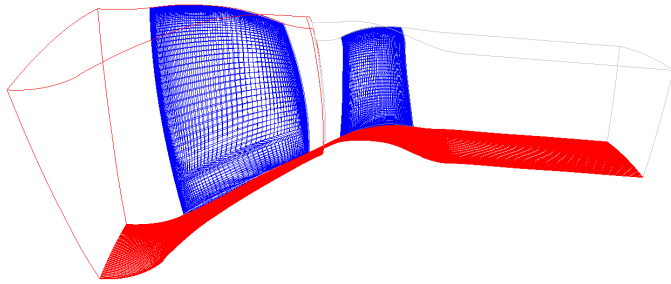
Figure 3. CRAC COMPUTATIONAL DOMAIN.

Rotor 2. The grids are actually stacked 2D grids on surfaces of revolution as shown in the meridional plane. Careful attention to the grid spacing as it exited Rotor 2 was made. Several grids were created, and flow features that are presented later were lost if the grid stayed too tight near the casing or if it fanned out too much. The number of grid cells used is based on prior work with TURBO described by Turner et al. [14]. Tangentially, the shock from Rotor 2 going upstream and the wakes from Rotor 1 going downstream needed to be resolved. The grids were not resolved as fine as those presented by List [12, 13]. Those simulations needed to resolve details of vortex shedding which was not expected to dominate the flow physics. As mentioned, the spanwise distribution is critical, and the number of cells is consistent with past validations.

The grids were partitioned using the TURBO pre-processor GUMBO. The Rotor 1 passage was partitioned into 48 blocks and the Rotor 2 passage was partitioned into 56 blocks, which efficiently splits the load among each processor.

Table 2. NUMBER OF CELLS FOR THE ROTOR PASSAGES.

	Rotor 1	Rotor 2
Number of Cells	1.58 million	1.89 million
Axial Cells	214	292
Blade to Blade Cells	82	72
Spanwise Cells	90	90

Initialization and Boundary Conditions

The isentropic inlet boundary condition was used. Values for the inlet to Rotor 1 were taken from the CRAC rig data gathered upstream of the IGV blade row. The total pressure, tangential angle and radial angle were also specified at the inlet, and these values came from an IGV solution using TURBO. A free-stream turbulence intensity of 4% was specified for this simulation. The
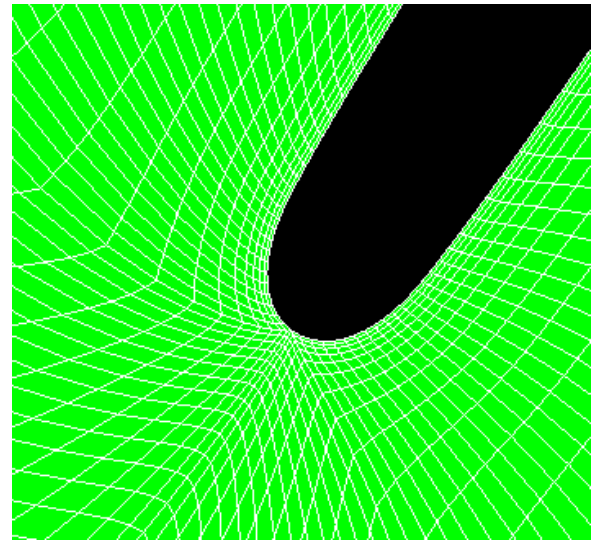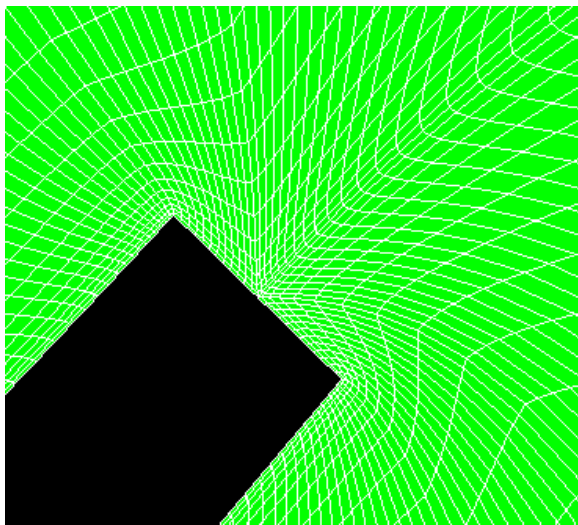

(a) Rotor 1
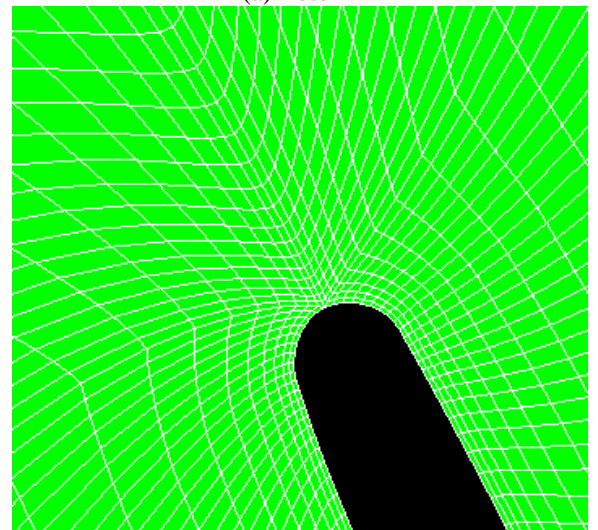
(b) Rotor 2

Figure 4. LEADING EDGES AT 50% SPAN.

numerical method for applying the inlet profile and the turbulence intensity by TURBO has been confirmed in the analysis. Between the two rotor blade passages an interface boundary condition was used. This boundary condition interpolates the flow solution in a time-accurate sense to the neighboring rotor passage grid.

The flow field was initialized at a uniform Mach number. At the exit, during the initial iterations a mass flow boundary condition was used followed by a static pressure boundary condition. The exit static pressure boundary condition was imposed as a uniform profile across the span which was possible due to the cylindrical endwalls and near-zero swirl at the exit plane.

(a) Rotor 1
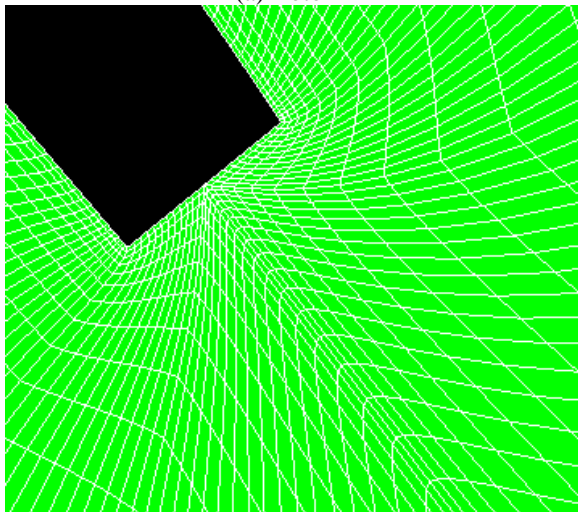
(b) Rotor 2

Figure 5.   TRAILING EDGES AT 50% SPAN.

The exit pressure boundary condition is based on a 1D extrapolation of all characteristics and imposition of the upstream-running characteristic using the specified pressure.

Aspiration Slot Simulation

The location of the source terms on the second rotor grid were defined by finding the Rotor 2 grid cell closest to the aspiration slot geometry. Figure 6 shows the aspiration slot laid over the grid. Each source term was given a magnitude based upon the overall aspiration through the slot and the fraction of the source cell area to the total area of the slot. The use of TURBO with source terms to simulate cooling flow is discussed by List and Turner [16]. The difference is that for cooling flows, the

sources need the mass, momentum, energy and turbulence equation sources. For the current simulation with suction, the sources are actually sinks and specified as a negative value. As such, the flow leaves the domain with the velocity, internal energy, and turbulence quantities in the cell with the sink. No values for momentum, energy, or turbulence sources need to be defined. The location of the source cells and their magnitudes were written to a file, which was then decomposed into blocks using a method similar to that of GUMBO. Slight modifications were made to TURBO to allow the decomposed source term files to be read in and applied to the simulation.
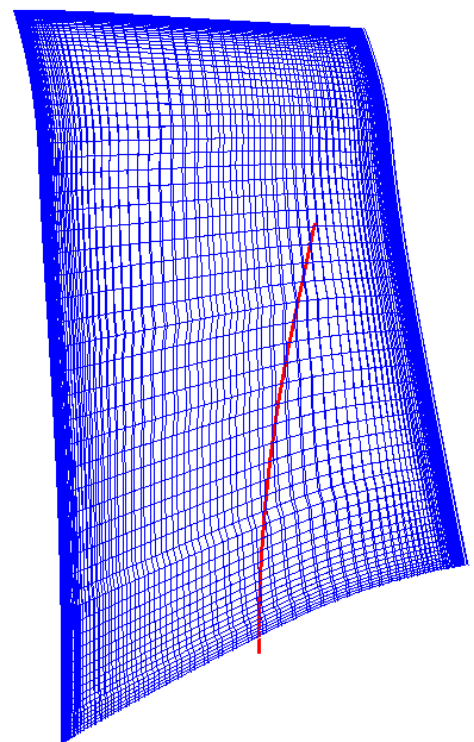

Figure 6.   AXISYMMETRIC VIEW OF THE ASPIRATION SLOT OVERLAID ONTO THE ROTOR 2 GRID.

Simulation Parameters

The simulation was run with a second order temporal accuracy and a third order spatial accuracy. TURBO employed six Newton sub-iterations with three Gauss-Seidel passes at each sub-iteration. The CRAC simulation was run with 160 time steps per Rotor 2 blade passing. The blade passing for a counter-rotating pair of rotors is based on the sum of the magnitude of the wheel speeds. The simulation was run at the Gas Turbine Simulation Laboratory at the University of Cincinnati, Center

Hill Research Center. For the simulation, 52 Pentium Core2Duo 2.4GHz CPUs were utilized. Due to the availability of processors, two simulations were run at the same time, one with aspiration terms and one without. Both simulations began with the mass flow exit boundary condition corrected by density, which was set at 24kg/sec to agree with experiment. These exit conditions were run for 15,000 iterations to allow the mass flows to rise to the boundary condition value. Both simulations were then run to a static pressure boundary condition of 155,025 Pa imposed across the span. After 10,000 iterations, aspiration effects were added to one of the runs by including the source terms into the simulation. The two simulations were run to convergence after which time averaged data was gathered. The time averaged data was then post-processed using APNASAcat, which averages circumferentially, and uses interpolation based on the conservative weights and pointers described by Kirtley et al. [17].

RESULTS
Convergence History

The convergence history of the mass flows at the inlet and exit of both rotors is shown in Figure 7(a). TURBO was initialized with a mass flow exit boundary condition. The mass flows increased until about 5000 iterations. At this point all four mass flows began a low frequency oscillation that had been seen in previous simulations. An immediate and significant drop in the mass flows is seen after switching to the pressure exit boundary condition. The mass flows increased steeply after about 1000 iterations. The mass flows settled out about 13000 iterations after the simulation was changed to the static pressure exit boundary condition. Two periods of the converged mass flows are illustrated in Figure 7(b). One period in this plot is 160 times 29 or 4640 iterations, and represents the time for all 29 blades in Rotor 2 to pass by the Rotor 1 passage. The mass flow at the exit of the second rotor has large oscillations, but on average is lower than the other three mass flows due to the aspiration. The three mass flows before the exit have a downward trend due to a low frequency oscillation. The low amplitude of the oscillation of the first three mass flows indicate the solution has converged. The large amplitude of the oscillation of the exit mass flow can be attributed to the imposition of the boundary condition.

After 100,000 iterations, the solution was run for 4640 more iterations while a time average was obtained for both the aspirated and non-aspirated case. Depending on the network load on the cluster and the stage of running, the solution with 52 processors takes approximately 3.3 seconds per iteration. This translates to about 4 days of wall clock time for a solution starting from scratch.

Numerical probes can be placed anywhere in the flowfield as TURBO runs. Many probes were placed, although four are presented here. They are all near the interface, and tangentially they are placed mid-passage. Two are in the Rotor 1 grid, and
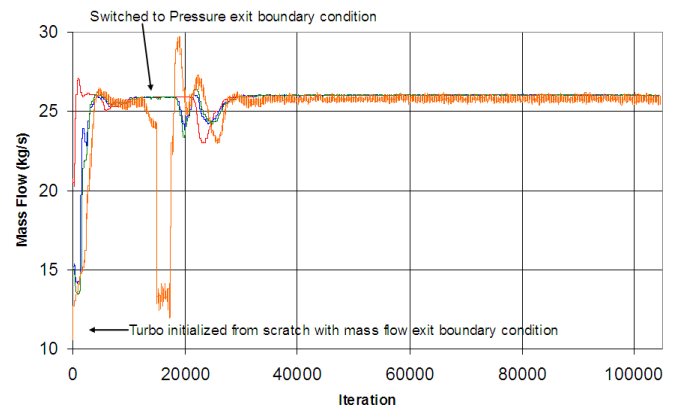
(a) Overall Mass Flow History
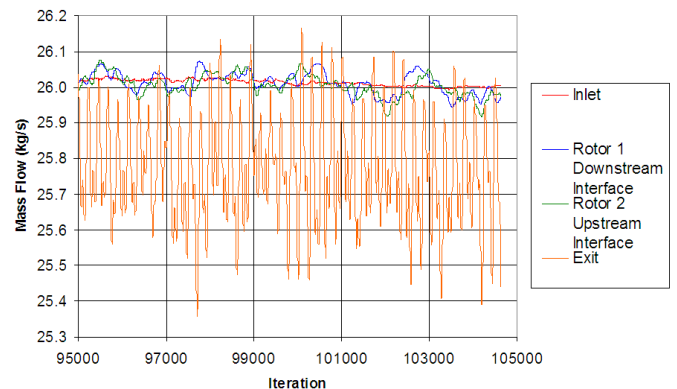
(b) Massflow Over Two Periods

Figure 7. MASS FLOW HISTORY.

two are in the Rotor 2 grid. Two are near mid-span, and two are very near the casing. The time response from these probes after 104,640 iterations are shown in Figure 8. The probe locations are shown in Figure 9 in the meridional plane. In addition to the probe locations, this figure shows the grid near the casing needed to resolve the flow features seen in the experiment. It had to be expanded, but not fanned out too much. The static pressure is plotted for probes 1 and 2 in Figure 8(a) which depicts the shock passing by from Rotor 2. Four Rotor 2 blade passings are shown for $4 \times 160 = 640$ iterations. The signal at midspan is periodic, but the casing is less so and shows some lower frequency content. The axial velocity is plotted for probes 3 and 4 for four Rotor 1 blade passings in Figure 8(b). This is for $4 \times 160 \times \frac{29}{20} = 4 \times 232 = 928$ iterations. The wake from Rotor 1 can be seen in this signal. Again the midspan probe is very periodic, whereas the one near the casing has lower frequency content. One of the issues with unsteady simulations is whether a periodic solution even exists. The experiment is a transient blowdown test. The simulation has been run long enough to get to a near-periodic solution. The time average must be done over a sufficiently long

6

time frame and over full dominant periods to provide a useful solution. This has been done in this case over 4640 iterations.

(a) Static Pressure in Rotor 1

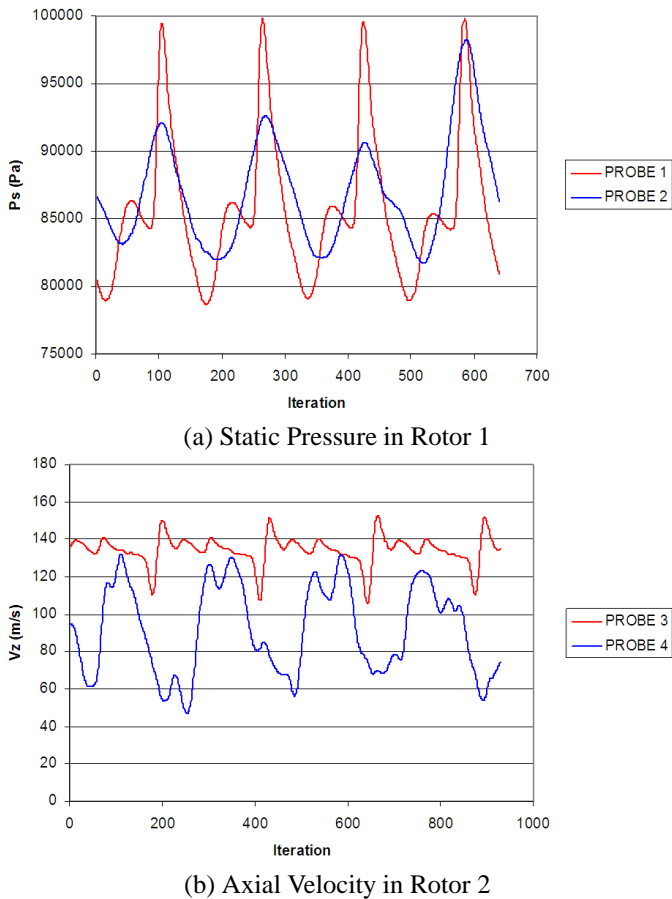
(b) Axial Velocity in Rotor 2

Figure 8. STATIC PRESSURE AND AXIAL VELOCITY NUMERICAL PROBE READINGS.

The time averaged solution has been post-processed to obtain axisymmetric averages and 1D averages. Figure 10(a) shows the 1D average of mass flow as a function of axial distance for both the aspirated and non-aspirated case. The non-aspirated case is essentially flat and represents the degree of convergence from periodic flow of this chosen period (the variation in mass flow is an indication of level of convergence and that the average has been taken over the right period of time). For one period of a converged periodic solution, the axisymmetric average 1D mass flow of the time average solution with no source or sink terms should be flat. For the aspirated case, the inlet flow is higher due to the mass flow extracted, and can be seen in the 1D variation. Rotor 2 is choked and sets the flow.

Comparison With Data

The 1D mass averaged total pressure and the area averaged casing static pressure are both plotted in Figure 10(b). It is clear that the shocks are further aft in both rotors for the aspirated case.

A profile at the measurement plane of mass-averaged values of PT and TT have been extracted as part of the axisymmetric averaging of the time-averaged solutions. These profiles are shown in Figure 11 along with the corresponding efficiency for the aspirated time averaged solution. In this figure are also the area averaged experimental and 3D design CFD results as presented by Parker [4]. The 3D design CFD results used the Average Passage code APNASA developed by Adamczyk [18].

The data spread exists because the design point was spanned by a range of time in the blowdown facility after the diaphragm was released. Near the tip the character of the experimental results with the efficiency rising is picked up by the current TURBO phase-lag simulation. This character of a kick-up in efficiency near the tip was also seen in a Air Force Research Lab test called SMI which was also picked up by TURBO as shown by Turner, et al [14]. The explanation for SMI was found to be a large amount of radial migration due to shed upstream vortices. The cause for the CRAC case is different, and will be explained more fully later.

The comparison of the efficiency is good, although the comparison of temperature and pressure that was actually measured is not as good. The efficiency is a good integrator, and does demonstrate that features are being captured and validates the method. The test had a lot of non-uniformities at the inlet that are not well enough know to be modeled. In addition, the slot was intended to pull flow uniformly along the span, but it is not known how well that was accomplished. Therefore it is likely in the experiment that the suction flow was different than that modeled in the simulation.

Comparison Between Aspirated and Non-Aspirated Simulation

A comparison of the 1D efficiency is shown in Table 3, and also shows the value calculated for the non-aspirated simulation. The efficiency is defined by

$$\eta = \frac{PR^{\frac{\gamma-1}{\gamma}} - 1}{TR - 1} \tag{5}$$

The comparison is good considering the simulation did not model the distortion upstream. The experimental values are area averaged quantities and do not include data from the endwalls. The TURBO simulations are mass averaged. The benefit of the aspiration is clear. Figure 12 shows a comparison of the exit profiles for the aspirated and non-aspirated simulation. The aspirated profiles are the same as those in Figure 11. Up and down

the span, the efficiency for the aspirated simulation is better. This is primarily due to a reduction in the total temperature. This is caused by a more efficient Rotor 1 and as explained below, the aspiration slot sucks off the high-temperature, high-entropy fluid for the entire span. The high total pressure for the non-aspirated case near the tip is most likely due to a pumping of fluid in a separated region behind the shock. This, however, is at high entropy so the total temperature is higher. The character of the efficiency that is seen in the data near the tip is not there for the non-aspirated simulation. It can be inferred therefore that it is due to the details of the aspiration.

Table 3. EFFICIENCY VALUES FOR EXPERIMENT AND SIMULATION.

	Efficiency	PR	TR
MIT Experimental	0.879	2.934	1.411
TURBO Aspirated	0.894	2.906	1.399
TURBO Non-aspirated	0.872	2.901	1.409

Figures 13, 14, and 15 show plots of 1D time-averaged values and axisymmetric contour plots of Mass Averaged Total Temperature, Mass Averaged Entropy and a blockage parameter. This blockage parameter is the aerodynamic blockage as defined by Turner [19]:

$$b_{aero} = \frac{\dot{m}}{b_{metal}\widehat{\rho}\left(\widehat{V}_z A_z + \widehat{V}_r A_r\right)} \quad (6)$$

where b_{metal} is the physical metal blockage and $\dot{m}$ is the mass flow. The other quantities ($\widehat{\ }$) are derived based on tangential-mass averages of total pressure, total enthalpy, and angular momentum, rV_θ. The area average of static pressure, radial momentum and axial momentum are also used along with the equation of state. This quantity, $b_{aero} = 1$ if there are no tangential variations. The leading and trailing edges of both rotors can be seen by a change of blockage in Figure 15. The 1D averages are obtained by spanwise averaging the 2D values of blockage. This quantity is similar to the term that exists experimentally when static pressure, total pressure, total temperature, and flow angles are measured when the flow rate is known. The system is over defined, and leads to a blockage parameter. The plot shows that the aspirated case has higher b_{aero} or lower blockage than the non-aspirated case. This blockage parameter is also a very good indicator to pick out important flow features.

Figure 13 is the 1D plot and contour plot of Mass and Time Averaged Total Temperature for both cases. The reduction in temperature is clear for the aspirated case. Figure 14 shows the 1D plot and entropy contours. It is clear from this that there is a reduction in the entropy for the aspirated case near the tip of Rotor 2. The entropy plots clearly shows the advantage of the aspiration. This is true for both rotors and not just the one aspirated.

The blockage b_{aero} is shown in Figure 15, and is very different for the aspirated and non-aspirated simulations. It is clear that there is an increase in b_{aero} just upstream of the aspiration slot of Rotor 2 for the aspirated case, and the overall level of b_{aero} is higher even in Rotor 1.

Time Averaged Results

Figure 18(a) shows a 3D view of the two rotors (forward looking aft) so the suction sides of both rotors can be seen. Static pressure contours are also shown for the aspirated case. The axisymmetric view of both blade rows are shown in Figures 16 and 17 for both the aspirated and non-aspirated cases. The shocks can be clearly seen in these figures again showing the shocks further aft for the case with aspiration.

Figure 19(a) shows the relative Mach number contours at midspan for both rotors. The direction of rotation is superimposed on the figure, and the relative size of each blade row has been maintained. The shocks in both rotors can be clearly seen. The vector triangles are shown in Figure 19(b) at the leading and trailing edges of both rotors. Rotor 1 trailing edge and Rotor 2 leading edge have the same absolute velocity vector. From the figure, the relative velocities entering and exiting the rotors can be clearly seen and compared to the blade geometry that is part of the relative Mach number plot.

A detail of the trailing edge of Rotor 2 at midspan is shown in Figure 18(b). The color indicates the radial velocity. The lower corner is the end of the suction surface, so the flow exiting the suction surface is going down, and the flow exiting the pressure side is going up. The velocity vectors show a classic recirculating region except for the flow at the suction side corner having a tangential component.

Rotor 2 was designed with aspiration to reduce the shock-boundary layer interaction. One of the attributes of the aspiration that was not anticipated is that high entropy fluid near the tip is getting ingested into the aspiration slot. This is shown in Figure 20(a) where the streamlines have been placed in the boundary layer upstream of the slot. As such, the streamlines stop at the slot location. A separated region can be seen entraining the fluid downward from the tip. Several other streamlines are bent with a lot of streamline curvature to flow down into the slot. It is clear from the profiles shown in Figure 11 as well as the contour plots of Total Temperature and Entropy in Figures 13 and 14 that there is a dramatic reduction in the tip entropy rise due to aspiration. The fact that the high entropy tip flows are brought down in span and sucked out is an unexpected feature. Figure 20(b) shows that without the suction, the streamlines just after the shock are cen-

trifuged out.

The wiggle near the tip seen in the profiles of Figure 11 are partially explained by Figure 20 where some of the high entropy fluid is pulled down in span due to the aspiration slot for the case with aspiration. This segregates the flow somewhat and produces the wiggle in the efficiency profile. When there is no aspiration, the high entropy fluid is all collected in the tip in a large region of the endwall. Another explanation of this is to look at the radial flux of entropy. This is defined as

$$s_{r-flux} = \frac{\int \rho V_r s dt}{\Delta t} \qquad (7)$$

This has been calculated in Rotor 2 for one Rotor 1 blade passing period, and is shown at 90% span for the case with and without aspiration in Figure 21. The reference entropy is defined such that the entropy is all positive. The sign of the radial entropy flux is therefore related to the net flux of entropy up and down the span. The large area of red (positive) on the suction side of Rotor 2 is a net entropy flux going radially upward shown in Figure 21(b) for the case without aspiration. This shows the entropy flux going up in span for the case of no aspiration, but not for the case with aspiration.

Time Accurate Results

A great deal can be gleaned from the time averaged solution and is a good indication of an accurate periodic-converged solution. However, there is a huge amount of information in the time accurate results. Two of the interesting features at the last time step run are shown in Figure 22(a) and (b). Respectively, these are contours of static pressure at midspan of Rotor 1, and contours of entropy at midspan of Rotor 2. The shocks from Rotor 2 are clearly seen in Figure 22(a) impinging on the trailing edge pressure surface of Rotor 1. Also clear is the spacing difference between the rotors. The entropy contours in Figure 22(b) clearly show the shed vortices from Rotor 1 going through the passage of Rotor 2. The reduction in entropy on the suction surface is due to the aspiration slot. The shed vortices in Rotor 2 can also be seen clearly.

Stall Margin

Experimentally, the CRAC design has considerable flow range and stall margin. A discussion by Kerrebrock, et al. [1] suggested that this could be due to stability arguments made by Cumpsty [20] related to the slope of the pressure rise characteristic where the steeper characteristic tends to damp out flow non-uniformities. It was argued that a counter-rotating design will have a characteristic slope that is at least 50% steeper than a conventional 2 stage design. Another possibility is based on the simple explanation of rotating stall also discussed by Cumpsty [20].

In this explanation, the stall cell or disturbance runs in a direction that incidence is increased. In a conventional two stage design, both rotors are traveling in the same direction so the disturbance rotates in the same sense as the rotors. For the counter-rotating design, the rotors are traveling in different directions. Therefore a disturbance is less likely to travel and disrupt the flow in the entire annulus. Parker, in his thesis [4] also describes the inlet distortion that has been seen in the experiment. Distortion will be very different from a phase shift of total temperature around the annulus relative to a total pressure distortion typical of conventional designs shown by Gorrell et al. [21]. This again will likely be due to particle paths in the absolute frame for the CRAC design being very different from a conventional design.

Another reason the stall margin was probably improved is due to the aspiration itself. The computational simulation has been performed with a phase lag boundary condition at a single operating point, and cannot address the characteristic, distortion or stall. However, the results already presented can be interpreted for relevance to improved stall margin. As shown in Figures 20 and 21 and explained earlier, the aspiration slot tends to pull high entropy flow down into the slot. This has the effect of cleaning up the tip flows and improving stall margin. Lei et al. [22] presented some work to quantify hub-corner stall. The effect of the aspiration slot near the hub is to postpone separation in the corner of the suction surface and the hub which again will have an improvement in stall margin.

Based on Figures 10(b), 16, and 18(a), one can see that the shocks in both Rotor 1 and 2 are further aft, and in a more choked position. For Rotor 2, this is because the aspiration slot sets the shock foot on the suction surface. For Rotor 1 it is because the mass flow is higher (due to suction) as seen in Figure 10(a). The effect is to give more stall margin which is related to the amount the shock moves forward and spills. The spillage is then typical of a near-stall condition. The effect is that stall margin is improved with no decrement in efficiency rather than in a full chocked condition where efficiency is greatly sacrificed.

CONCLUSIONS & FUTURE WORK

A time accurate simulation of the MIT Counter-rotating aspirated compressor has been made both with and without aspiration. Comparison with data of the aspirated solution was good, especially near the tip picking up detailed features of the measured profile. On a 1D basis, the experimental efficiency is 87.9%, and the aspirated simulation is 89.4%. A comparison between the aspirated and non-aspirated simulations shows the aspirated simulation is 2.2% higher in efficiency than the non-aspirated case. Flow details of the time-averaged solution in the second rotor were presented which show dramatic radial migration of high entropy fluid from the tip that gets ingested into the suction slot.

This and other flow details shed light on the improved flow

range and stall margin of the counter-rotating aspirated design.

Future work will be centered on looking at throttling the compressor to look at off-design. A full annulus simulation of all three blade rows, the IGV, Rotor 1, and Rotor 2 is also planned to better explain the good stall characteristics observed experimentally and to explore distortion.

ACKNOWLEDGMENT

REFERENCES

[1] Kerrebrock, J. L., Epstein, A. H., Merchant, A. A., Guenette, G. R., Parker, D., Onnee, J.-F., Neumayer, G., Adamczyk, J. J., and Shabbir, A., 2006. "Design and test of an aspirated counter-rotating fan". In ASME Turbo Expo 2006. ASME Paper GT-2006-90582.

[2] Merchant, A., Kerrebrock, J. L., and Epstein, A. H., 2004. "Compressors with aspirated flow control and counter-rotation". In 2nd AIAA Flow Control Conference. AIAA Paper no. 2004-2514.

[3] Merchant, A. A., 2002. "Aerodynamic design and performance of aspirated airfoils". In ASME Turbo Expo 2002. ASME Paper GT-2002-90582.

[4] Parker, D. V., 2005. "Design and operation of a counter-rotating aspirated compressor blowdown test facility". Master's thesis, Massachusetts Institute of Technology, Cambridge, MA, June.

[5] Chen, J. P., and Whitfield, D. L., 1993. "Navier-Stokes Calculations for the Unsteady Flowfield of Turbomachinery". AIAA Paper no. 1993-0676.

[6] Chen, J., Celestina, M. L., and Adamczyk, J. J., 1994. "A new procedure for simulating unsteady flows through turbomachinery blade passages". In ASME Turbo Expo 1994. ASME Paper no. 94-GT-151.

[7] Chen, J. P., Ghosh, A. R., Sreenivas, K., and Whitfield, D. L., 1997. "Comparison of computations using navier-stokes equations in rotating and fixed coordinates for flow through turbomachinery". In 35th Aerospace Sciences Meeting and Exhibit. AIAA Paper no. 97-0878.

[8] Chen, J. P., and Barter, J., 1998. "Comparison of time-accurate calculations for the unsteady interaction turbomachinery stage". AIAA Paper no. 98-3292.

[9] Chen, J. P., and Briley, W. R., 2001. "A parallel flow solver for unsteady multiple blade row turbomachinery simula-tions". In ASME Turbo Expo 2001. ASME Paper no. 2001-GT-0348.

[10] Zhu, J., and Shih, T. H., 2000. CMOTT Turbulence Module for NPARC. Contract Report NASA CR 204143, NASA Glenn Research Center, Lewis Field, OH.

[11] Gorrell, S. E., Car, D., Puterbaugh, S. L., Estevadeordal, J., and Okiishi, T. H., 2006. "An investigation of wake-shock interactions in a transonic compressor with digital partical image velocimetry and time-accurate computational fluid dynamics". *Journal of Turbomachinery,* **128**, October, pp. 616–626.

[12] List, M. G., Gorrell, S. E., Turner, M. G., and Nimersheim, J. A., 2007. "High fidelity modeling of blade row interaction in a transonic compressor". In 43rd AIAA/SAE/ASME Joint Propulsion Conference. AIAA Paper no. 2007-5045.

[13] List, M. G., 2007. "Quarter annulus simulations of blade row interaction at several gaps and discussion of flow physics". Master's thesis, University of Cincinnati, Cincinnati, OH, August.

[14] Turner, M. G., Gorrell, S. E., and Car, D., 2005. "Radial Migration of Shed Vortices in a Transonic Rotor Following a Wake Generator: A Comparison Between Time Accurate and Average Passage Approach". *ASME Paper GT2005-68776.*

[15] Kamp, M. A., Nimersheim, J., Beach, T., and Turner, M. G., 2007. "A turbomachinery gridding system". In 45th AIAA Aerospace Sciences Meeting and Exhibit. AIAA Paper 2007-18.

[16] List, M., Turner, M., Remotigue, M., Chen, J., and Veres, J., 2004. "Unsteady cooled turbine simulation using a pc-linux analysis system". In 42nd AIAA Aerospace Sciences Meeting and Exhibit. AIAA Paper no. 2004-0370.

[17] Kirtley, K. R., Turner, M. G., and Saeidi, S., 1999. "An average passage closure model for general meshes". ASME Paper 99-GT-077.

[18] Adamczyk, J. J., Celestina, M. L., Beach, T. A., and Barnett, M., 1990. "Simulation of 3-dimensional viscous flow within a multistage turbine". *Journal of Turbomachinery,* **112**(3), July, pp. 370–376.

[19] Turner, M., Norris, A., and Veres, J., 2003. "High fidelity 3d simulation of the ge90". In 33rd AIAA Fluid Dynamics Conference and Exhibit. AIAA Paper no. 2003-3996.

[20] Cumpsty, N. A., 4002. *Compressor Aerodynamics.* Krieger Publishing Company, Malabar, FL.

[21] Gorrell, S. E., Yao, J., and Wadia, A. R., 2006. "Unsteady rans analysis of distortion transfer and generation".

[22] Lei, V.-M., Spakovszky, Z. S., and Greitzer, E. M., 2006. "A criterion for axial compressor hub-corner stall". In ASME Turbo Expo 2006. ASME Paper GT-2006-91332.
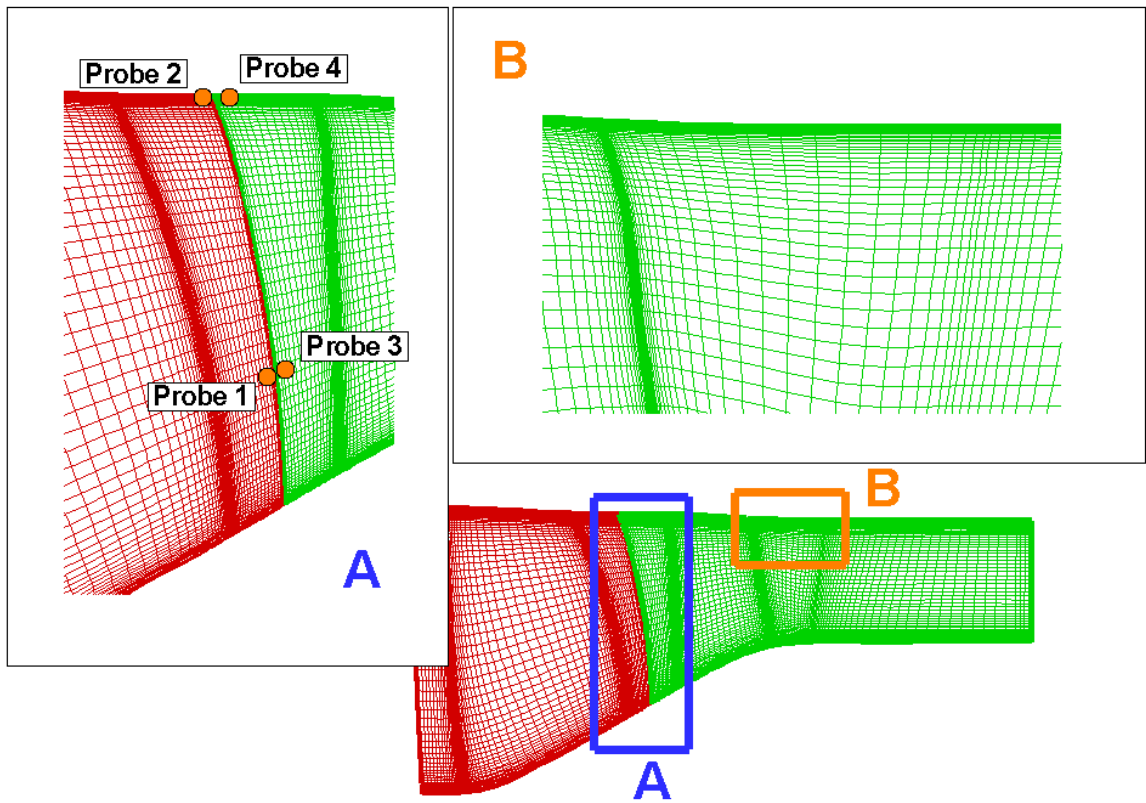
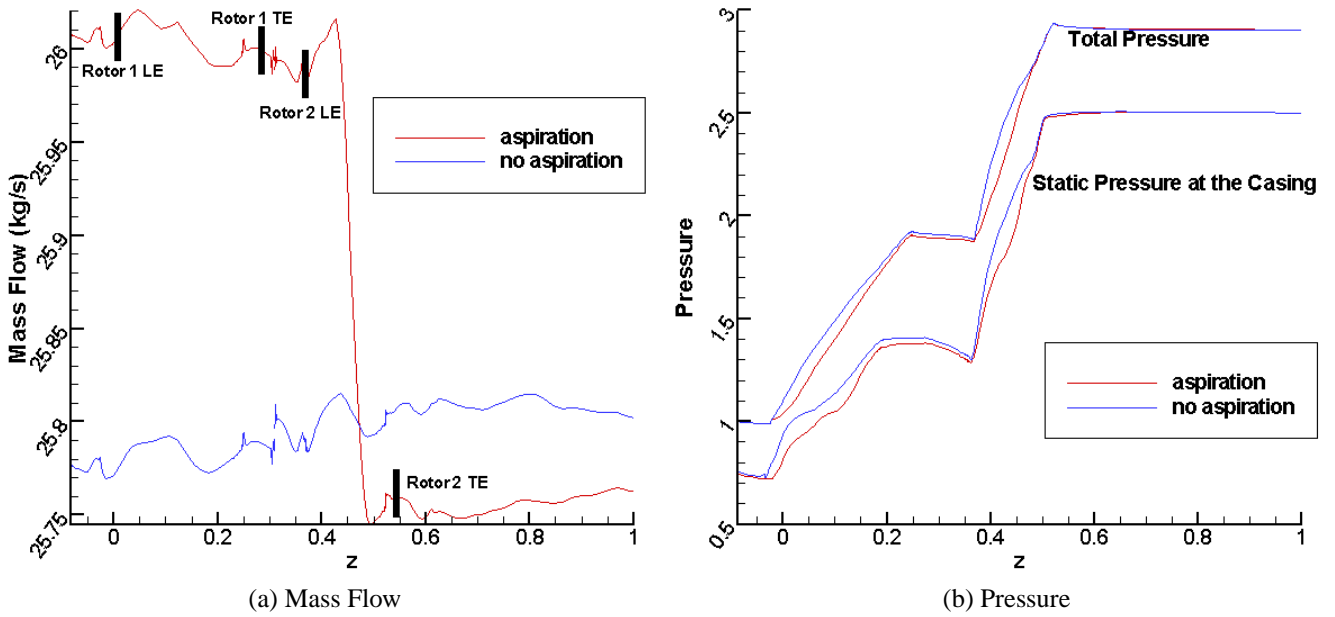Figure 9. NUMERICAL PROBE POSITIONS FOR CAPTURING TIME ACCURATE READINGS FOR STATIC PRESSURE AND VELOCITY.

(a) Mass Flow

(b) Pressure

Figure 10. 1D TIME AVERAGED MASSFLOW AND PRESSURE LINE PLOTS.

11

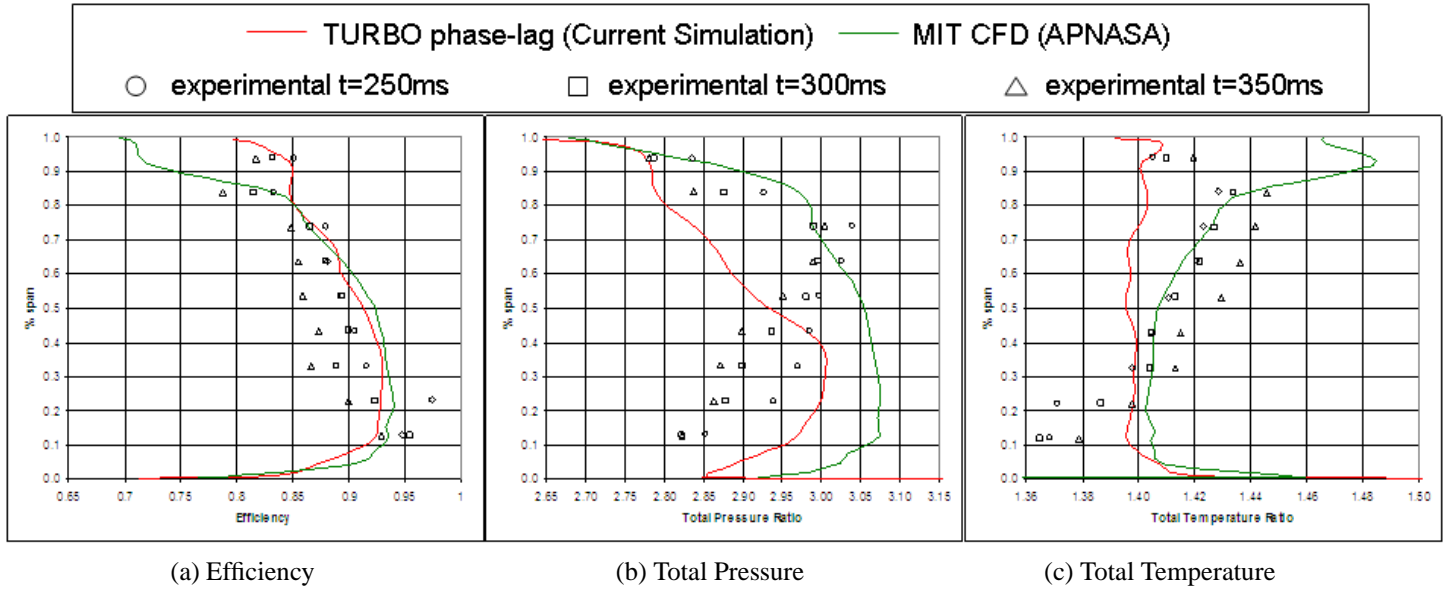(a) Efficiency   (b) Total Pressure   (c) Total Temperature

Figure 11. COMPARISON OF EFFICIENCY, TOTAL PRESSURE AND TOTAL TEMPERATURE BETWEEN MIT EXPERIMENTAL AND CFD DATA AND TURBO PHASE-LAG DATA.
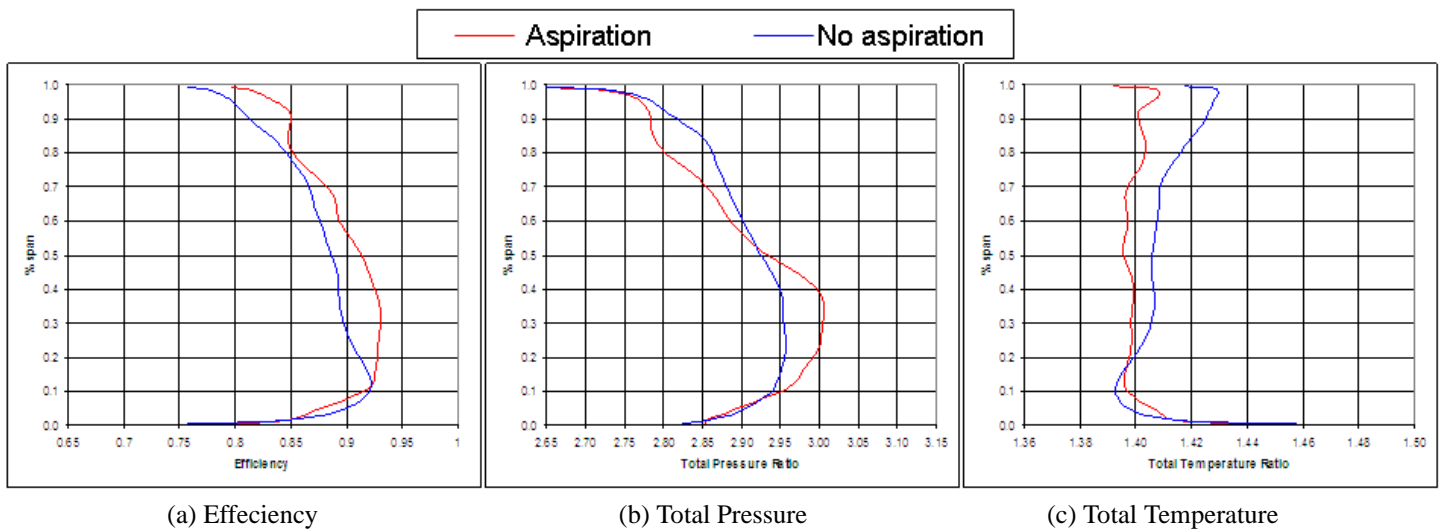

(a) Effeciency   (b) Total Pressure   (c) Total Temperature

Figure 12. COMPARISON OF EFFICIENCY, TOTAL PRESSURE AND TOTAL TEMPERATURE BETWEEN ASPIRATION AND NON-ASPIRATION CASES USING TURBO PHASE-LAG SIMULATION.
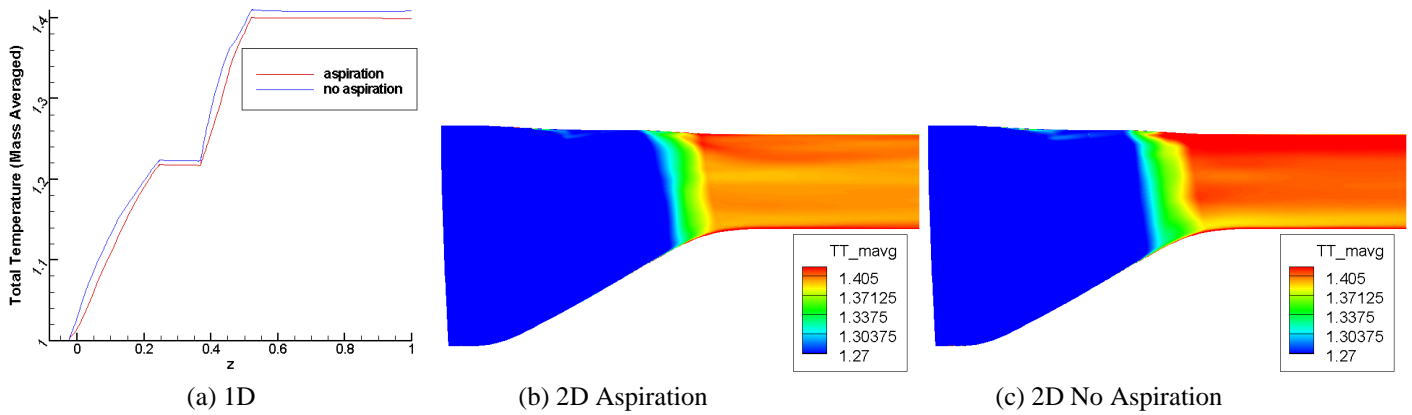
Figure 13.   1D LINE PLOTS AND 2D TIME AVERAGED AND CIRCUMEFERENTIALLY AVERAGED TOTAL TEMPERATURE CONTOURS.
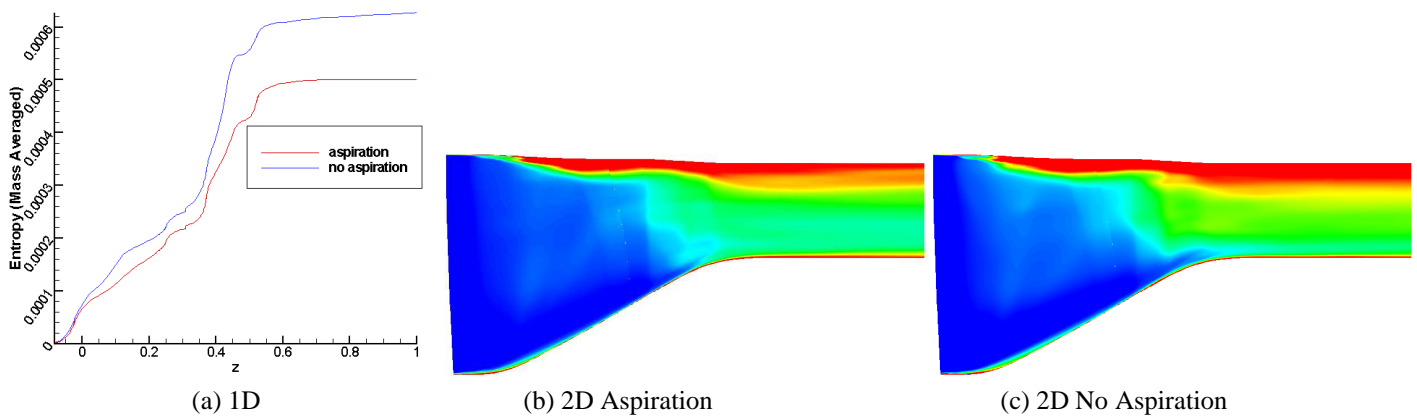
Figure 14.   1D LINE PLOTS AND 2D TIME AVERAGED AND CIRCUMFERENTIALLY AVERAGED ENTROPY CONTOURS.
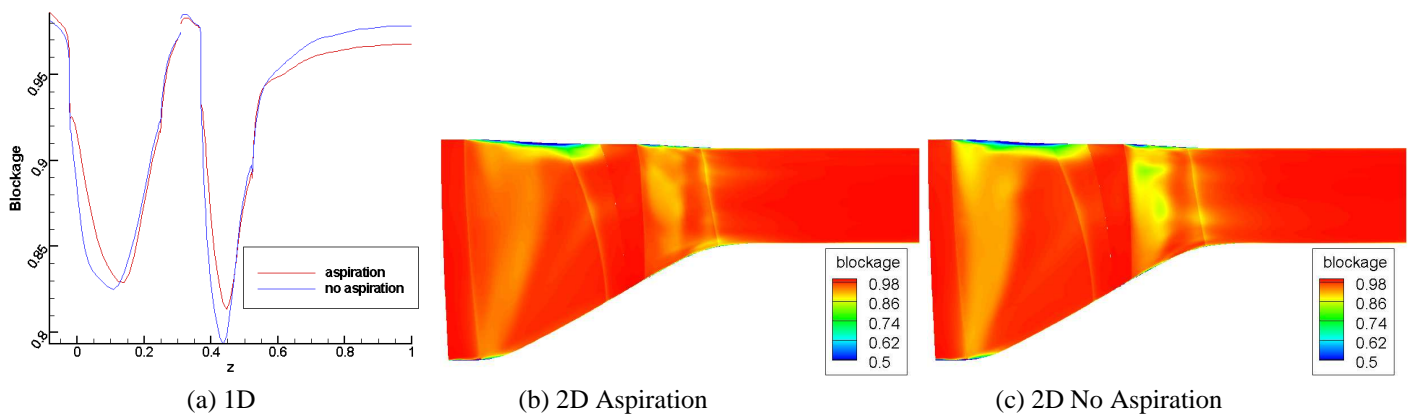
Figure 15.   1D LINE PLOTS AND 2D TIME AVERAGED AND CIRCUMFERENTIALLY AVERAGED BLOCKAGE CONTOURS.

(a) Aspiration (b) No Aspiration
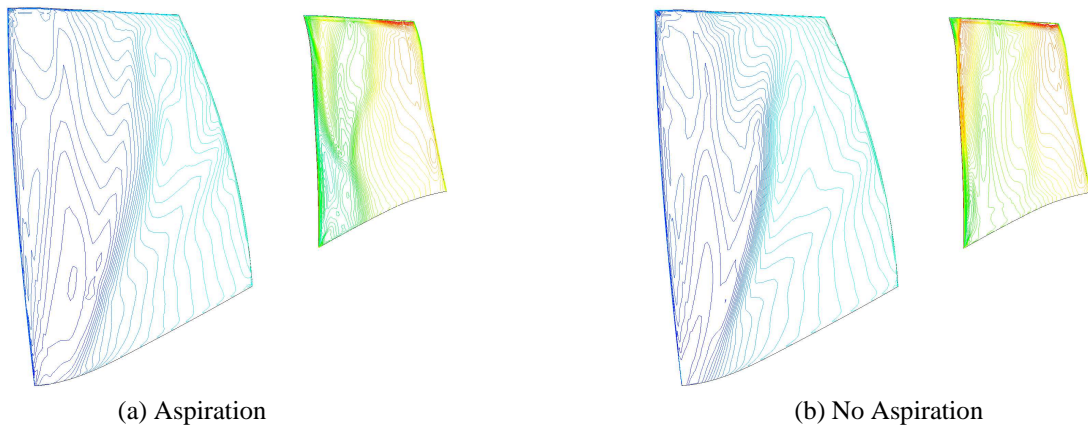
Figure 16.   AXISYMMETRIC VIEW OF THE TIME AVERAGED ASPIRATED SOLUTION WITH STATIC PRESSURE CONTOURS OF SUCTION SIDE OF ROTOR 1 AND PRESSURE SIDE OF ROTOR 2.
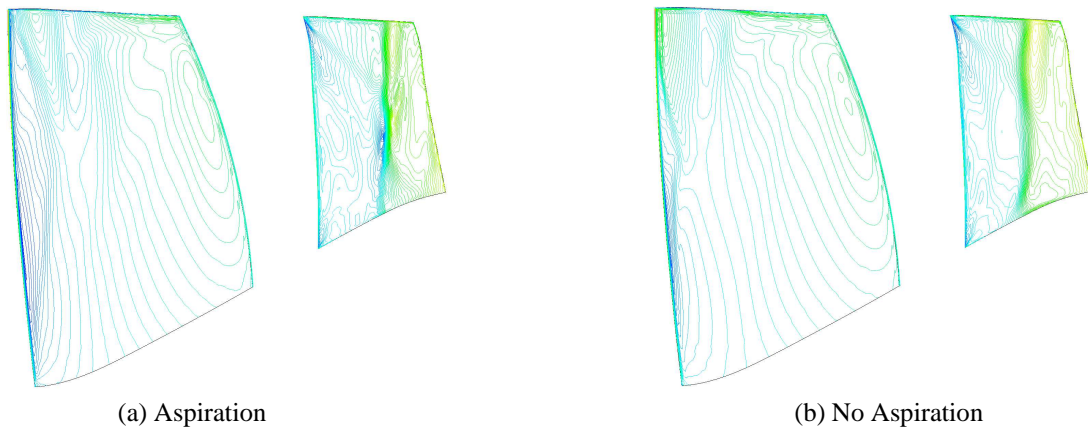

(a) Aspiration (b) No Aspiration

Figure 17.   AXISYMMETRIC VIEW OF THE TIME AVERAGED ASPIRATED SOLUTION WITH STATIC PRESSURE CONTOURS OF PRESSURE SIDE OF ROTOR 1 AND SUCTION SIDE OF ROTOR 2.
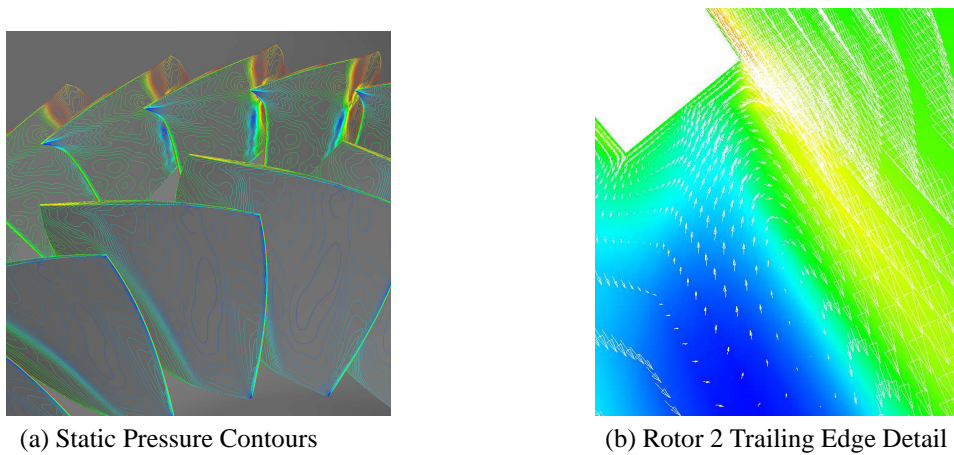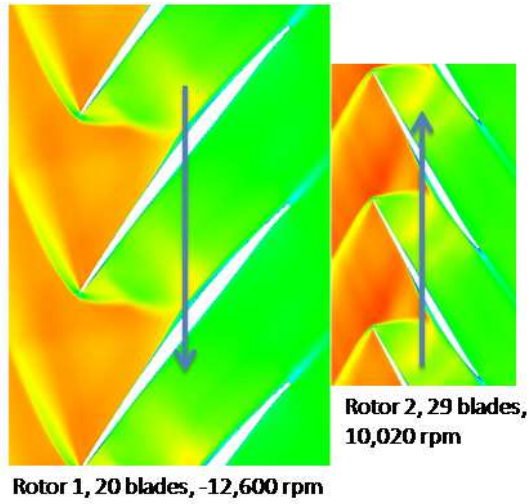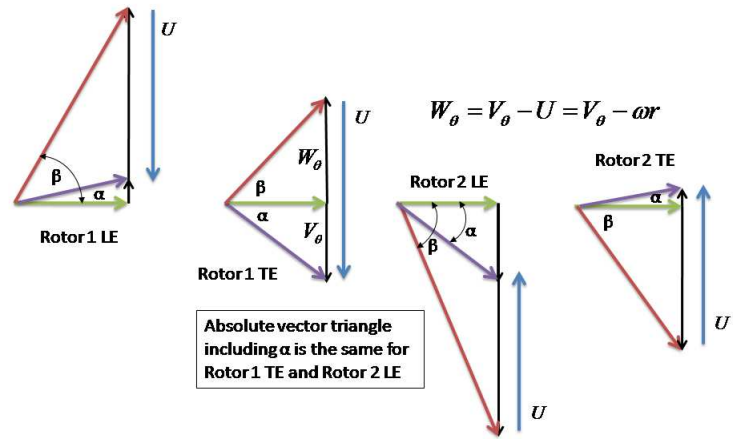

(a) Static Pressure Contours (b) Rotor 2 Trailing Edge Detail

Figure 18.   FLOW FEATURES. TIME AVERAGED STATIC PRESSURE CONTOURS OF THE ASPIRATED SOLUTION AND VELOCITY VECTORS AT THE TRAILING EDGE OF ROTOR 2

(a) M_{rel} at midspan

(b) Vector triangles

Figure 19.   RELATIVE MACH NUMBER AND VECTOR TRIANGLES FOR BOTH ROTORS.
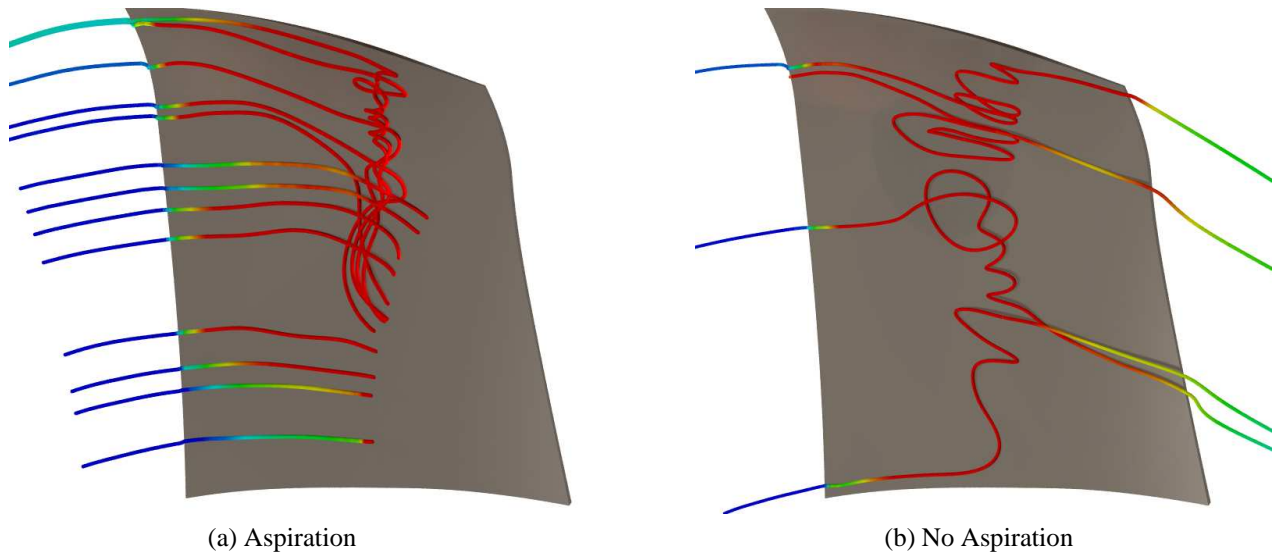

(a) Aspiration

(b) No Aspiration

Figure 20.   STREAMLINES GENERATED JUST OFF SUCTION SURFACE OF ROTOR 2 OF THE TIME AVERAGED ASPIRATED AND NON-ASPIRATED SOLUTION. COLORS SHOW ENTROPY WITH HIGH VALUES BEING RED. THE SUCTION SLOT IN THE ASPIRATED CASE CAUSES THE HIGH ENTROPY TIP FLOWS TO GET SUCKED IN AND REMOVED FROM THE FLOW.
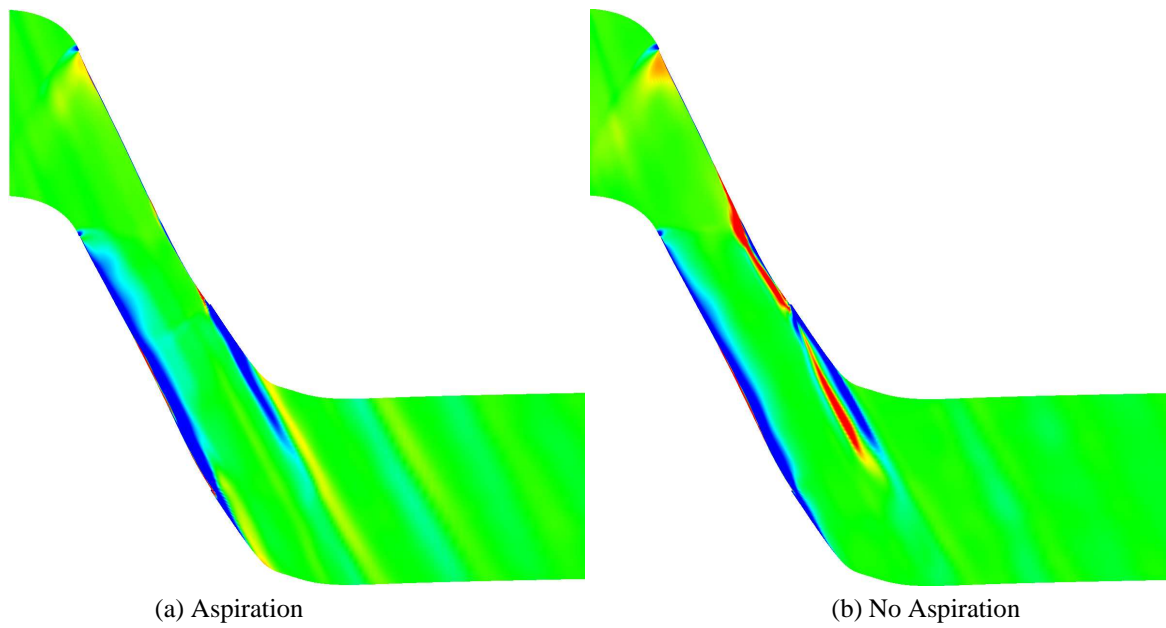
(a) Aspiration

(b) No Aspiration

Figure 21. RADIAL FLUX OF ENTROPY AT 90% SPAN DEFINED AS $\rho V_r s$. THE RED IS POSITIVE VALUES OF RADIAL FLUX. LESS ENTROPY MOVES UPWARD IN SPAN IN THE ASPIRATED CASE.

(a) Static Pressure at Midspan
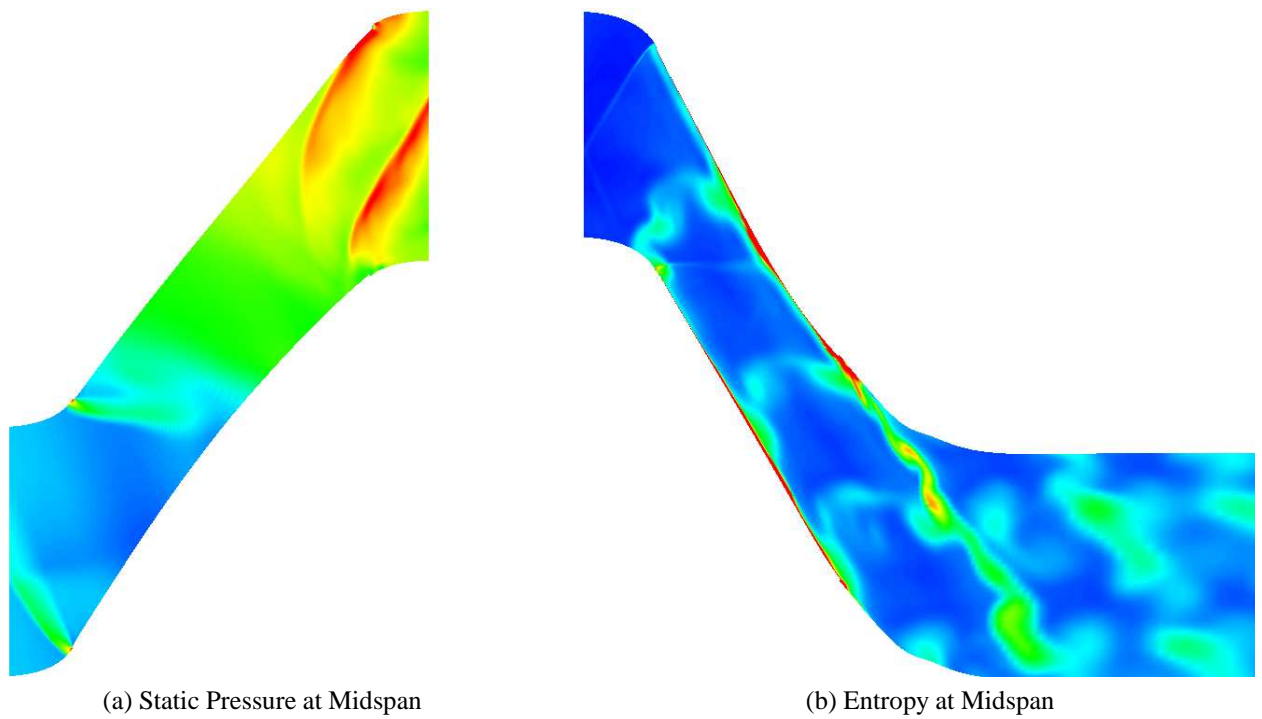
(b) Entropy at Midspan

Figure 22. CONTOURS OF STATIC PRESSURE AT MIDSPAN OF ROTOR 1 AND CONTOURS OF ENTROPY AT MIDSPAN OF ROTOR 2 AT TIME STEP 104640.